Understanding the Microscopic Origin of the Contact Resistance at the Polymer−Electrode Interface

Kalyani Patrikar,* V. Ramgopal Rao, Dinesh Kabra, and Anirban Mondal*

Cite This: https://doi.org/10.1021/acsami.3c10260 · Read Online
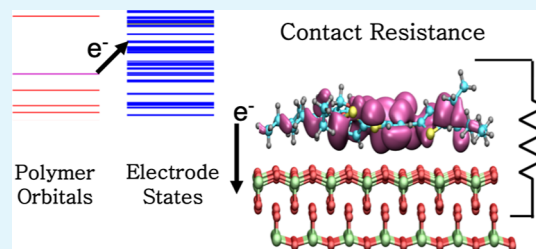
ACCESS | Metrics & More | Article Recommendations | Supporting Information

ABSTRACT: Contact resistance (R_C) in organic devices originates from a mismatch in energy levels between injecting electrodes and organic semiconductors (OSCs). However, the microscopic effects governing charge transfer between electrodes and the OSCs have not been analyzed in detail. We fabricated transistors with different OSCs (PTB7, PCDTBT, and PTB7−Th) and electrodes (MoO_3, Au, and Ag) and measured their contact resistance. Regardless of the electrodes, devices with PTB7−Th exhibit the lowest values of R_C. To explain the trends observed, first-principles computations were performed on contact interfaces based on the projector operator diabatization method. Our results revealed that differences in energy levels and the electronic couplings between OSCs' highest occupied molecular orbitals and vacant states on the electrodes influence device R_C. Further, based on values obtained from the first-principles, the rate of charge transfer between OSCs and electrodes is calculated and found to correlate strongly with trends in R_C for devices with different OSCs. We thus show that device R_C is governed by the feasibility of charge transfer at the contact interface and hence determined by energy levels and electronic coupling among orbitals and states located on OSCs and electrodes.

KEYWORDS: contact resistance, organic transistors, projector operator diabatization, density of states, electronic coupling, electron transfer rate

1. INTRODUCTION

Devices of organic semiconductors (OSCs), such as organic field effect transistors (OFETs), have led to several unique applications in recent times, such as flexible memories or wearable sensors.[1,2] However, these devices are less efficient than their inorganic counterparts, in part due to high operating voltages.[3] One rationale for this is the resistance at the interface of the semiconductor channel and source/drain electrodes in the device, known as contact resistance (R_C).[4,5] R_C acts in series with the channel's resistance and hence adds to the device resistance, lowering the device current in the process. As reducing channel length lowers channel resistance but not R_C, a high R_C limits the scaling of the device further.[6] Hence, a low R_C is required for both obtaining high device current at low voltage and enabling scaling of organic devices.

R_C is primarily caused by the mismatch of energy levels at the interface—the difference between Fermi energy of injecting electrode and ionization potential of p-type OSCs yields a barrier to hole injection from the electrode to the OSC during device operation.[7] Further, it is known that a dipole gets set up at the contact interface during equilibrium due to microscopic phenomena accompanying interface formation, such as pillow effects, defect generation, and induction of interface states.[8,9] The interface dipole repels the injecting hole, hence appending the injection barrier, and further increases R_C. The role of energy levels in reducing contact resistance has been reported, and it has been shown that employing electrodes with high work function,

carbon-based electrodes, or interlayers at the contact interface reduces R_C.[8,10,11] However, the role of microscopic interactions of OSC molecules with electrodes at interfaces in determining the R_C has not been explored in particular. It has been shown that orbital interactions at the interface significantly contribute to governing charge transport at the interface.[12,13] Especially, hole injection involves an electron extraction from the highest occupied molecular orbital (HOMO) of the OSC by the electrode. Therefore, the HOMO energy level and distribution are anticipated to be critical in affecting the charge-transfer process.

Analytical models have been developed to represent contact resistance in operational devices.[14,15] According to the power law description, it has been shown that the effect of parameters such as gate voltage can be explained based on the disorder and energy distribution inherent to OSCs. However, the role of microscopic interactions in determining the resistance at the interface has not been significantly explored. First-principles computations have been employed to probe the energetics affecting the electron transfer process between polymers and

electrodes.[16,17] Density functional theory (DFT)-based computations allow simulation of a monomer of OSCs and its interface with the electrode.[18] As the electron is transferred from HOMO of the OSC to vacant states of the electrode, the energy level of vacant states with respect to HOMO as well as electronic coupling between vacant states and HOMO are essential factors governing the hole injection process.[19] The effect of these variables can be combined to calculate the rate of electron transfer from HOMO to the bands of vacant states. However, comprehensive studies, including both the effects of energy levels and orbital interactions on electron transfer across the interface and understanding their effect on device R_C, have not been performed.

In this study, we demonstrate the role of electronic coupling between the OSC and electrode and the respective energy levels in explaining observed trends in device R_C. R_C is measured for OFETs combining different OSCs and electrodes. OFETs of p-type conjugated polymers such as PTB7, PCDTBT, and PTB7−Th are fabricated. These polymers have been used in high-efficiency solar cells and have displayed high mobility in polymer OFETs.[20−26] Other device parameters have also been reported to improve with the evolution of molecular design, including R_C.[5] The factors involving differences in molecular structures leading to improved device performance have not been explored in detail. For all three OSCs, three sets of devices were fabricated, with source-drain electrodes of MoO_3, Au, or Ag, which have been employed as electrodes for several organic devices due to both their high work function and ability to be deposited as thin films by methods such as physical vapor deposition.[27,28] Along with transistor characteristics, R_C was measured for all OFETs by the transfer length method. To understand the microscopic origins of the trends observed in R_C for different contact interfaces, first-principles computations were performed for all OSC−electrode combinations based on the projection-operator diabatization (POD) method.[29] The POD method has been shown in ref 18 to be an effective way to obtain electronic coupling between localized orbitals of organic molecules and delocalized states of periodic systems such as electrode thin films. The POD method has been used here to determine the energy of OSC orbitals, the vacant states on electrodes, and the electronic coupling between them. These parameters determine the electron transfer process between the respective entities during device operation. The electron transfer rates were estimated based on these values as per the Marcus−Hush equation.[19,30] Trends in values of electron transfer rates were analogous to those in R_C, showing that the combined effect of energy levels on the OSC and electrode and the electronic coupling between them are vital factors determining device behavior for contact interfaces. Hence, it is shown that the rate of charge transfer is a holistic parameter, combining energy levels and electronic coupling effects that explain the effect of microscopic processes on the resistance of the given interface in the device.

2. METHODS

2.1. Experimental Methods.
Devices were fabricated on low resistivity p-Si substrates, which acted as Gate electrodes. To form the dielectric, the Si was thermally oxidized to form 200 nm SiO_2 on its surface; 100 nm PMMA was spin-coated on the oxide layer and annealed at 200 °C to render it insoluble. This bilayer dielectric has been shown to lead to more stable organic devices. Polymers poly[N-9′-heptadecanyl-2,7-carbazole-alt-5,5-(4′,7′-di-2-thienyl-2′,1′,3′-benzo-thiadiazole)] (PCDTBT), poly4,8-bis[(2-ethylhexyl)oxy]benzo[1,2-b:4,5-b′]dithiophene-2,6-diyl3-fluoro-2-[(2-ethylhexyl) carbonyl]-

thieno[3,4-b]thiophenediyl (PTB7), and poly[2,6′-4,8-di(5-ethylhex-ylthienyl) benzo[1,2-b; 3,3-b]dithiophene]3-fluoro-2[(2-ethylhexyl)-carbonyl]thieno[3,4-b]thiophenediyl (PTB7−Th) were obtained in powder form from Sigma-Aldrich. All polymers were spin-coated on the bilayer dielectric in an MBraun N_2 glovebox from 10 mg mL^{-1} solutions in chlorobenzene held at 60 °C and annealed after spin coating at 60 °C for 15 min. Electrodes were deposited by thermal evaporation at a vacuum of 3×10^{-6} mbar through stencil masks with channel lengths in the range of 75−200 μm to define the location and dimensions of the source and drain. Further, Ag electrodes have been used in hole-transporting organic devices and are considered a low-cost replacement for Au; thus, Ag is included in this study to identify factors affecting its performance as a hole-injecting electrode.[31] Here, devices were fabricated with Au, MoO_3, and Ag electrodes to compare the microscopic interactions at the contact interfaces and correlate with the measured contact resistance. In the case of Au or Ag electrodes, a 45 nm layer of metal was evaporated. For devices with MoO_3, a 40 nm layer of Ag was deposited on the MoO_3 layer without breaking the vacuum to maintain the stability of the electrode. The device stack was fabricated based on the protocol optimized by us previously.[22] Electrical measurements were carried out by a semiprobe station with a Kiethley 4200 SCS system.

2.2. Computational Methods.
Electronic structure calculations were based on DFT.[32,33] The polymer-electrode systems were initially optimized for each polymer and electrode surface. The polymer was represented by a single monomer unit as charge transport in OSCs occurs with temporal localization over a molecule. The electrode was simulated as four-layered slabs in the case of Au and Ag or three-layered slabs in the case of MoO_3. During the geometry optimization, the last two layers were held frozen, while the remaining atoms were allowed to be moved. Freezing the last two layers allowed it to represent the bulk of the electrode which did not interact with the OSC; meanwhile, the mobile surface layers were free to interact with the OSC. Geometry optimization was performed by applying the threshold conditions on the gradient of the electronic wave functions and the force on the nuclei with convergence criteria of 10^{-7} and 10^{-4} a.u., respectively. This was followed by calculations based on the POD method, with the entire molecule defined as a single block and the complete electrode slab defined as another block. Calculations were carried out using the Quickstep module provided by the CP2K program.[34,35] Exchange−correlation potentials were treated within the generalized gradient approximation employing the Perdew−Burke−Ernzerhof functional.[36] The energy cutoff was set to 415 Ry for the auxiliary plane wave expansion of the charge density. Valence electrons were modeled explicitly, whereas core electrons have been treated with norm-conserving Goedecker−Teter−Hutter (GTH) pseudopotentials.[37,38] Basis set TZ-GTH was employed for calculating systems with Au electrodes as it has been well optimized for organic-Au systems.[37,38] A TZV2P-MOLOPT-SR basis set was employed for systems with Ag electrodes. For the MoO_3 electrodes, the DZVP-MOLOPT-SR basis set was used.[39] For the remaining elements, a triple-ζ valence plus polarization basis set was adopted to expand the wave functions. Fermi−Dirac distribution smearing with an electronic temperature of 298.15 K was employed, involving metal surface calculations to preserve the fractional occupation of states near the Fermi energy. The Brillouin zone was integrated with a reciprocal space mesh consisting of only the gamma point. Properties of the blocks, such as energy levels and the electronic coupling among all states of donor and acceptor, were obtained by invoking the ET_Coupling module in the Properties section of CP2K, resulting in the energy level diagram of donor, acceptor, and complex as well as the electronic coupling between orbitals of donor and states of the acceptor. Reorganization energy was calculated by the four-point method.[40] For each OSC, the ground-state geometry of neutral and cation monomers was optimized, followed by energy calculations for charged and neutral monomers in neutral and charged geometry, respectively. Separate calculations were performed for this purpose using package Gaussian09[41] at the B3LYP level of theory using a basis set 6-31G(d,p).[42−46] Using the output of energy levels, electronic coupling, and reorganization energy, the rate of
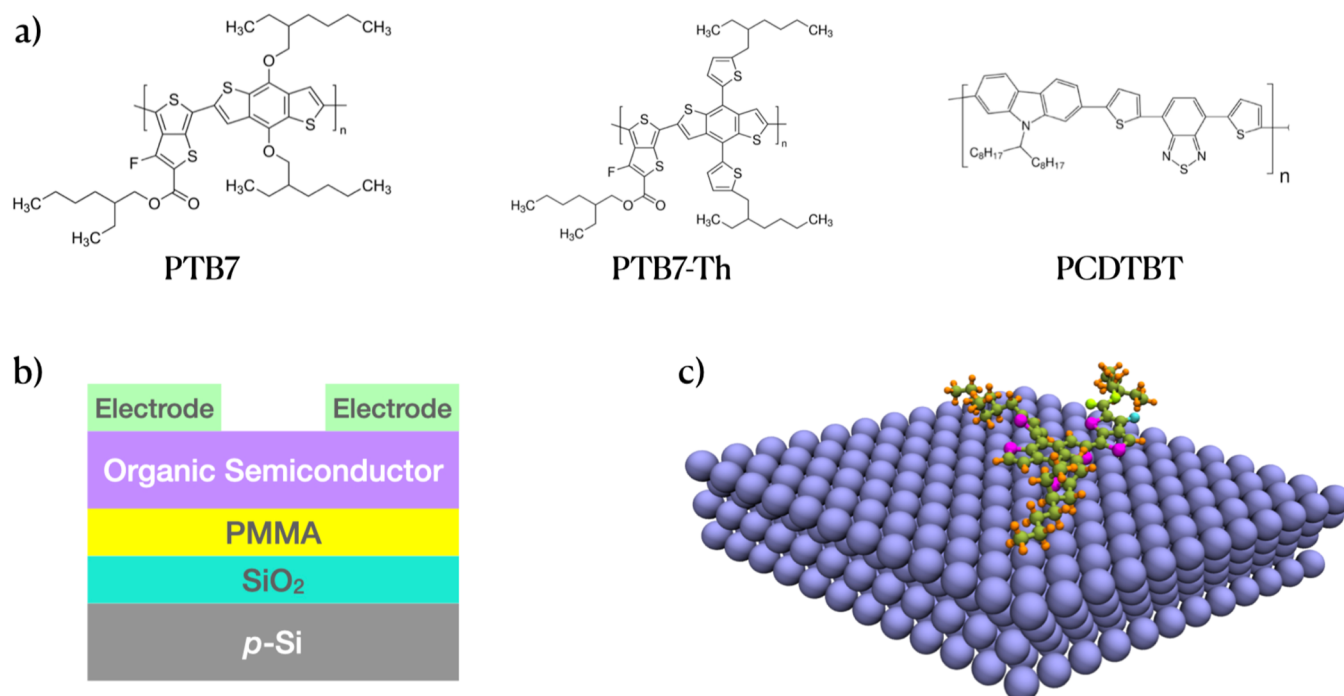
Figure 1. (a) Chemical structures of p-type polymer semiconductors. (b) Generic transistor architecture employed in this study to fabricate devices. (c) Representative electrode-polymer structure deployed in electronic structure calculations.
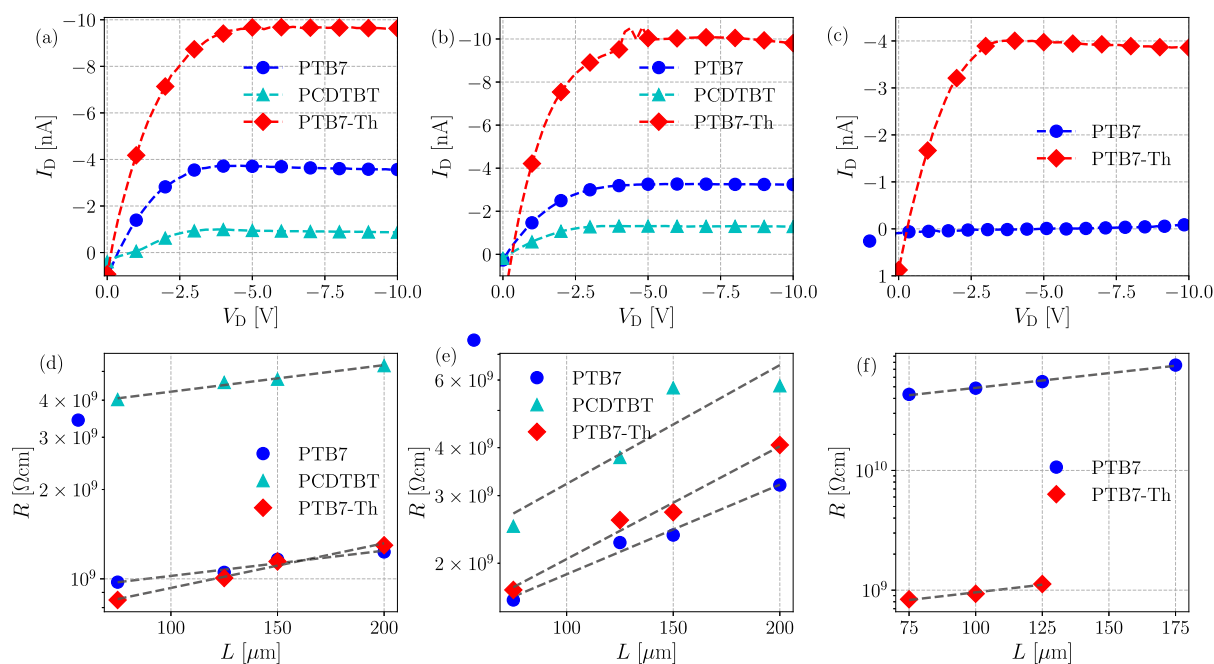

Figure 2. $I_D - V_D$ for OFETs comprising PTB7, PCDTBT, or PTB7−Th as the OSC with electrodes (a) Au, (b) MoO₃, and (c) Ag, showing the trends among OSCs. R_C extracted from $I_D - V_D$ for OFETs with different L values for all OSCs, with electrodes (d) Au, (e) MoO₃, and (f) Ag.

electron transfer between polymers and electrodes can be evaluated as per the Marcus−Hush equation as given in eq 1.[19,30]

$$k_{ET} = \frac{2\pi}{\hbar} \int J_{DA}^2(E) \frac{1}{1 + \exp\frac{E - E_F}{kT}} n(E) \frac{1}{\sqrt{4\pi\lambda kT}}$$

$$\exp\frac{-(\lambda - \Delta E + q\eta)^2}{4\lambda kT} dE \qquad (1)$$

Here, E_F is the Fermi level of the system, λ is the reorganization energy of the polymer, $n(E)$ is the number of states at energy level E, and η is the overpotential of the electrode. The function was integrated over E of all vacant energy levels, with ΔE obtained as the difference between the appropriate energy level of the donor and E. λ was obtained for all three OSCs via DFT calculations simulating the geometry of neutral and cation monomers formed due to electron transfer. $J_{DA}(E)$ refers to the electronic coupling strength between the relevant donor orbital and states at energy level E. To obtain $J_{DA}(E)$, the average electronic coupling for OSC HOMO and all degenerate states with energy E was calculated. η was considered zero for all systems as accurate information regarding its value for the OSC−electrode systems cannot be obtained at this stage.
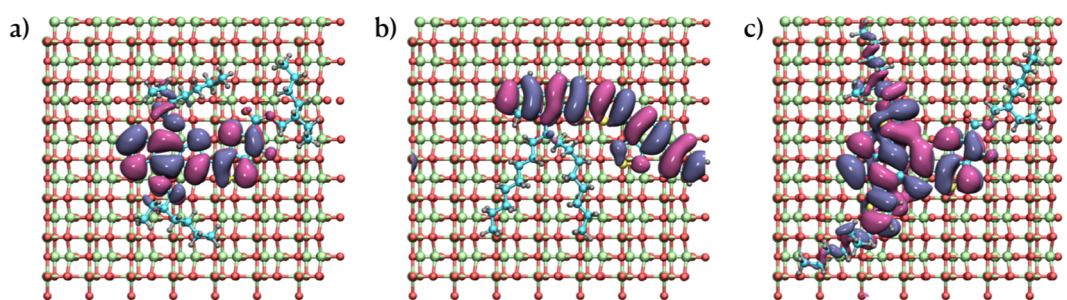
C

Figure 3. Localized HOMO orbitals of (a) PTB7, (b) PCDTBT, and (c) PTB7−Th monomers on the MoO$_3$ surface.

3. RESULTS AND DISCUSSION

3.1. Device Characteristics. OFETs based on p-type polymers, namely, PTB7, PCDTBT, and PTB7−Th, were fabricated, and their device characteristics were measured. The molecular structures of all polymers are illustrated in Figure 1a. OFETs were fabricated with these OSCs, with a top electrode configuration as shown in Figure 1b, combined with source-drain electrodes of MoO$_3$, Au, or Ag. Figure 2a−c shows output characteristics $(I_D − V_D)$ of all OFETs with a channel length (L) of 75 μm, at the gate voltage (V_G) set at −5.0 V. For devices with Au electrodes, it is apparent that the drain current (I_D) for PTB7−Th is the highest, while that of PCDTBT is the lowest. Saturation I_D for PTB7−Th OFETs is 9.0 nA, while it is 1.2 nA for OFETs of PCDTBT. The saturation current is intermediate in the case of PTB7, at 3.8 nA. Similar trends can be observed in the case of OFETs with MoO$_3$ electrodes. The device current for PTB7−Th is the highest, and it is the lowest for PCDTBT. For OFETs with MoO$_3$ electrodes, saturation I_D for PTB7−Th is 9.8 nA, higher than both PTB7 OFETs at 3.8 nA and PCDTBT at 1.6 nA. In the case of OFETs with Ag electrodes, devices with PTB7−Th have a saturation I_D of 4.0 nA, while it is 0.2 nA for PTB7. As devices with PCDTBT have values of I_D lower than 0.1 nA, which is close to the noise margin in measurements, they are not considered further.

To evaluate the resistance at the contact interface independently from the channel, we obtained R_C from device characteristics by the transfer length measurement method. As R_C and channel resistance (R_{Ch}) are in series, the total resistance of the device (R) is a sum of R_C and R_{Ch}. While R_{Ch} is a function of L, R_C is only a property of the interface and does not depend on L, as exhibited in eq 2.[47]

$$R = R_{Ch} + 2R_C = L\frac{1}{WC\mu(V_G − V_T)} + 2R_C \qquad (2)$$

Here, W is the width of the OFET channel, C is the capacitance of the dielectric, and V_T is the threshold voltage. Accordingly, plotting R, as estimated from $I_D − V_D$ characteristics of devised OFETs at low drain voltage values (V_D) against L, yields a linear graph. The y-intercept of the linear fit, an extrapolation to $L = 0$, represents the total R_C arising at the source and the drain. Resistance (R) values obtained from $I_D − V_D$ curves are plotted for OFETs with varying channel lengths (L). The best linear fit of R vs L is obtained to extract contact resistance from its y-intercept. Consistency was maintained by plotting the most stable devices on the same substrate for all OFETs. Figure 2d−f shows the plots of R (measured at $V_G = −5.0$ V) against L for all of the designed OFETs. The channel lengths are uniform for all cases; however, in the case of devices with PTB7−Th−Ag, the channel lengths are not >125 μm, and the same channel lengths have been plotted for devices of PTB7−Ag. For OFETs with Au

electrodes, R vs L is shown in Figure 2d. As evident, R_C of PTB7−Th is the lowest at 3.38×10^8 Ωcm, while it is highest for PCDTBT at 3.31×10^9 Ωcm and intermediate for PTB7 with 6.81×10^8 Ωcm. Figure 2e displays the same profiles for OFETs with the MoO$_3$ electrodes. The highest R_C observed is for the OFET of PTB7 at 7.45×10^8 Ωcm, while the lowest is again in the case of OFET of PTB7−Th at 1.48×10^8 Ωcm. In comparison, the PCDTBT-based device exhibits R_C at an intermediate range of 4.17×10^8 Ωcm. In the case of OFETs with Ag electrodes, as shown in Figure 2f, the R_C for PTB7−Th OFET at 3.27×10^8 Ωcm is markedly lower than that of OFET of PTB7 at 1.64×10^{10} Ωcm. Values of R_C for all OFETs are summarized in Table S1 of the Supporting Information. R_C of PTB7−Th OFETs are in the range of values reported previously.[48,49] To the best of our knowledge, there are no reports of contact resistance with pristine PTB7 and PCDTBT OFETs with similar device configurations. It has been seen that the OFET mobility is affected by the contact resistance of the device due to the difference in charge carrier density injected in the channel.[50] Channel mobility (μ) is obtained from the slope of $R − L$ plots according to eq 2 as shown in Figure S2 with respect to R_C. In general, high mobility coexists with low contact resistance. However, it cannot be stated that there is a clear correlation between μ and R_C due to variations in factors such as trap density and material disorder for different devices. We note that R_C for PTB7−Th is the lowest among all of the OSCs regardless of the electrodes. This indicates that the OSC molecular structure, electrode material, as well as interfacial interactions between the OSC and the electrode have a significant influence over interface resistance. To explain the observed trends in R_C, the process of hole injection, and microscopic factors determining the resistance at the interface, simulations on the contact interface were conducted.

3.2. Simulation of a Contact Interface. Structures comprising the monomer of an OSC and the electrode film were simulated, as shown in Figure 1c. Performing first-principles calculations on such a slice of the contact interface enabled the assessment of microscopic phenomena isolated from bulk effects. The POD method allows entities within a system to be defined as donors and acceptors, thereby defining the electron transfer process. Futera and Blumberger have developed an algorithm to implement POD-based calculations for periodic systems to enable an accurate simulation of electron transfer between molecular and thin-film entities.[18] Properties of the donor, acceptor, and entire complex are calculated for all OSC−electrode systems using the POD scheme implemented in the CP2K program.

During the device operation, a hole is injected from the electrode to the polymer molecule by electron transfer from the OSC HOMO to vacant electrode states. Similarly, electron

injection in *n*-type devices will involve electron transfer from occupied states of the electrode to the lowest unoccupied molecular orbital (LUMO) of the OSC. Figure 3 shows the distribution of HOMO on the monomers as calculated for the polymer−electrode systems by first-principles. It is evident that the orbital is highly delocalized over PTB7−Th, occupying the entire conjugated segment as well as segments of the side chain. In the case of PTB7, the orbitals are localized over the conjugated segment and only to pendant groups linking side chains; the extent of delocalization is less than for PTB7−Th. In contrast, the HOMO spreads over the entire conjugated segment but not the side chains in PCDTBT. Similar trends for the delocalization of HOMO are observed for systems with polymers and Au or Ag electrodes. For OFETs with any electrode, the trends in values of R_C correlate with the extent of orbital delocalization over the polymer. The extent of delocalization of HOMO increases interactions between the orbital of the polymer and electrode. To quantify the effect of delocalization of orbitals on device behavior, further calculations are performed to obtain HOMO energy levels of the OSC, and energy levels of vacant states of electrodes and electronic coupling between them were calculated to understand the process of electron transfer between the OSC and the electrode.

The POD method was employed to calculate all energy levels for the polymer and electrode systems. Energy levels computed for the monomer donor, electrode acceptor, and those for the donor−acceptor complex for systems of all polymers with MoO_3 are shown in Figure 4. Red lines represent the energy levels of the polymer, the entire system is in green, and the acceptor is indicated with blue lines. HOMO and the next higher LUMO level of the polymer are marked as cyan lines, while the first vacant state of the electrode is marked in orange, such that all acceptor states plotted above the line represent vacant states. A black line marks the Fermi level of the complex. The HOMO level is the highest energy level for all three polymers above the Fermi level. Further, there are vacant states on the electrode with energy levels in proximity to the HOMO level of the polymer, which favor electron transfer. In the PTB7−MoO_3 system, the HOMO energy (E_H) is −0.256 eV, while the energy of the lowest vacant state on the electrode (E_L) is −0.174 eV. Thus, the minimum energy difference between the HOMO energy and available vacant states is −0.082 eV. Further, there are four degenerate states available at this energy level. In the PCDTBT−MoO_3 system, E_H is −0.316 eV while E_L is −0.158 eV, thus leading to a higher minimum energy difference of −0.157 eV, with four degenerate states. For the PTB7−Th−MoO_3 system, while E_H is −0.114, E_L is −0.149 eV, making the energy difference 0.035 eV, with two degenerate states available. In this case, the lowest vacant state is at a lower energy level than HOMO, energetically favoring the downhill electron transfer. While the performance of PTB7−Th with other oxide electrodes can only be gauged with the computation of the density of states, we expect it to have a low contact resistance due to the contribution of its delocalized orbital, which is a molecular property. The energy level diagrams for OSC−Au and OSC−Ag systems are shown in Figure S1 of the Supporting Information. While the difference between E_H and E_L is negative for all systems with Ag electrodes, it is positive for systems with Au electrodes, favoring electron transfer more. The values of E_H and E_L for all OSC−electrode systems are summarized in Table S1 of the Supporting Information.

An electron is transferred from the HOMO of the OSC to vacant states of the electrode, with the energy difference
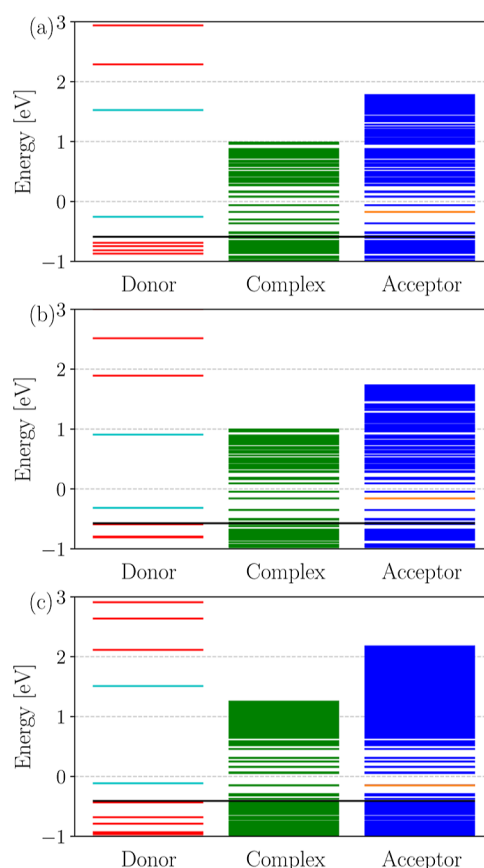

Figure 4. Energy level diagram displaying states of donor OSC (red), OSC−electrode complex (green), and electrode acceptor (blue) for OSC−MoO_3 systems: (a) PTB7, (b) PCDTBT, and (c) PTB7−Th. The OSC donor has discrete levels corresponding to molecular orbitals, while the acceptor has energy bands with degenerate states at each energy level. Cyan lines mark donor HOMO and LUMO, and the lowest vacant state on the acceptor is marked by an orange line such that all levels above the orange lines represent vacant states on the acceptor.

between the participating states (ΔE) being one of the factors determining the feasibility of the transfer. However, other than a low difference in energy levels, electronic coupling between the states is necessary for electron transfer. Electronic coupling (J_{DA}) for each vacant state on the acceptor electrode with the HOMO of the donor OSC calculated by the POD method is shown in Figure 5 for all OSC−electrode systems. Each energy level (E) containing vacant states on the electrode is represented by the energy difference $\Delta E = E_H − E$. Thus, if $\Delta E > 0$ (<0), the downhill (uphill) electron transfer is facilitated (hindered) due to the location of the HOMO level being higher (lower) in energy than the states at E. Degenerate states of any E may have a different coupling strength with the OSC HOMO. In the case of OSC−MoO_3 systems, the range of electronic coupling is lower than that of OSC−Au and OSC−Ag systems for all OSCs. However, in all OSC−MoO_3 systems, a high electrode state density is available with low ΔE. Thus, while the electronic coupling strength is low between donor HOMO and acceptor states, hence lowering the feasibility of electron transfer to any particular state, many states are available, increasing avenues for electron transfer. OSC−Au systems possess a high density of states at low ΔE accompanied by increased values of J_{DA}, which is reflected in the low values of R_C for OFETs with Au electrodes as well as the higher difference between OFETs of all three
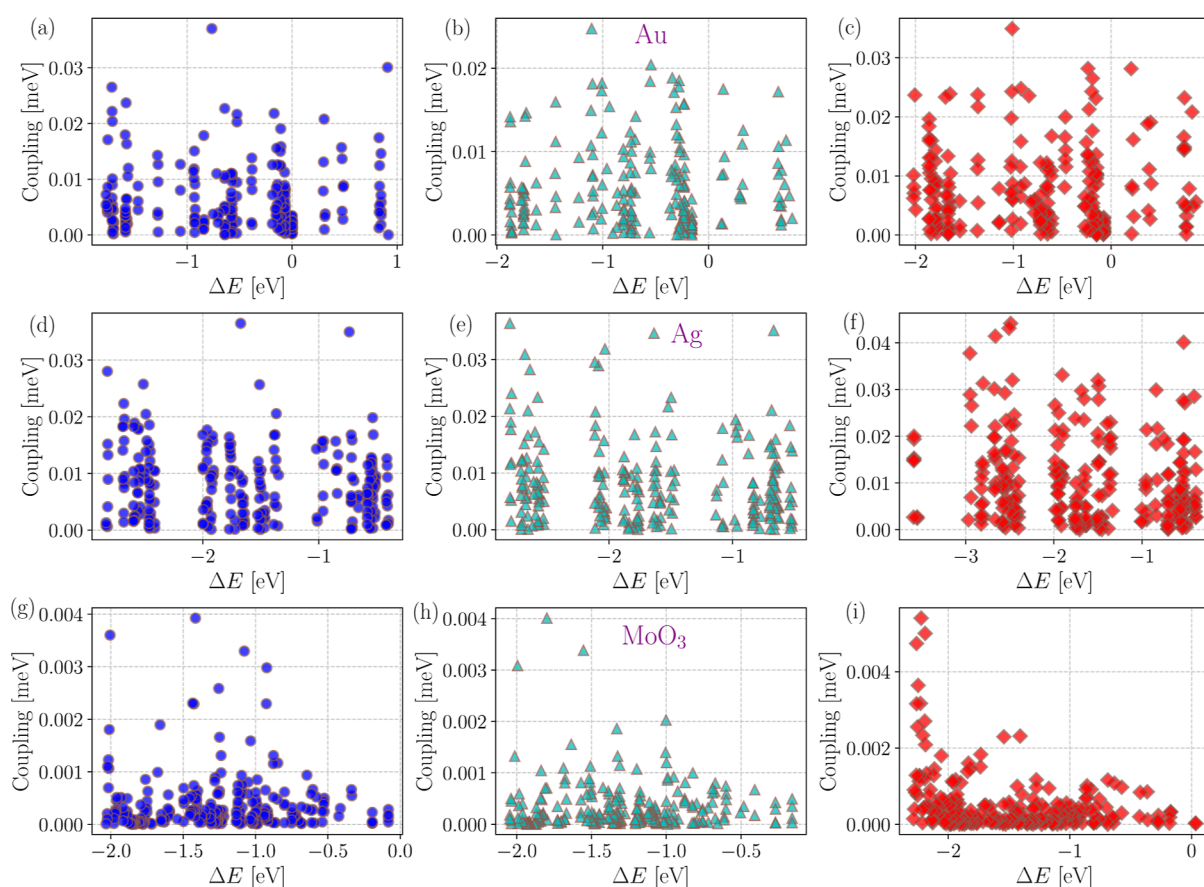
Figure 5. Electronic coupling values between HOMO (E_H) and vacant acceptor states (E) for all OSC−electrode systems: (a−c) Au, (d−f) MoO$_3$, and (g−i) Ag electrodes. In all rows, the system's OSC sequence is displayed as PTB7, PCDTBT, and PTB7−Th. On the x-axis, ($E_H − E = \Delta E$) are plotted to exhibit the variations in available states for electron transfer in different systems. Electronic coupling between donor HOMO and all degenerate states for each E are plotted on the y-axis.

OSCs. In the case of OSC−Ag systems, while the values of J_{DA} are higher than for OSC−MoO$_3$ systems and comparable to those of OSC−Au systems, ΔE is significantly higher too. In this case, the large energy gap between donor HOMO and acceptor states hinders electron transfer even though their electronic coupling is high. Thus, the combination of the energy difference and electronic coupling determines the feasibility of electron transfer from the donor HOMO to an acceptor state. The electron transfer rate is calculated to evaluate the effect of these parameters on R_C quantitatively.

3.3. Electron Transfer Rates. The rate of electron transfer k_{ET} from the OSC to the electrode is obtained for all OSC−electrode systems as per the Marcus−Hush equation (see eq 1). Figure 6 exhibits the correlation between the computed electron transfer rate and the measured R_C of OFETs with the respective OSC−electrodes at the contact interface. It is not accurate to compare values of k_{ET} across different electrodes as the value of η is not available. However, trends are visible for all of the systems for a given electrode. We observe that R_C decreases with an increase in k_{ET} calculated for the respective OSC−electrode system. For devices with OSC−Au and OSC−MoO$_3$ contact interfaces, the decrease in R_C is linear, with an increase in k_{ET} when viewed on a logarithmic scale. Values of k_{ET} for all OSC−electrode systems are summarized in Table S1 of the Supporting Information.

In the case of calculating values of k_{ET}, which involves summing up a function of J_{DA}, ΔE, and n over all the available states, k_{ET} is high when a high J_{DA} and n are combined with a low

ΔE. In some cases, low J_{DA} is compensated by high n available at levels with low ΔE, or vice versa. Thus, k_{ET} captures the effects of interactions between the OSC and the electrode on electron transfer. For OFETs with Au electrodes, computed k_{ET} is high in magnitude due to high values of J_{DA} and n combined with low ΔE, an effect which is highest for PTB7−Th−Au, leading to the lowest R_C among all devices. In the case of the PTB7−Au system, while states at lower ΔE are available, there are fewer states overall, lowering the k_{ET}. For PCDTBT−Au, the range of values of J_{DA} is lower than that of PTB7−Au and PTB7−Th−Au, yielding relatively lower k_{ET}. In the case of OSC−MoO$_3$ systems, low values of J_{DA} are compensated for by high n and low ΔE, leading to intermediate values of k_{ET} as compared to systems with Au and Ag electrodes, as is the case for R_C of OFETs with OSC−MoO$_3$ contact interfaces. For the PTB7−Th−MoO$_3$ system, n is higher than for PTB7 and PCDTBT, leading to higher k_{ET}, which correlates with its low R_C. The values of J_{DA}, n, and ΔE are in a similar range for all OSC−MoO$_3$ systems, reflected in the small range of values of R_C for OFETs with MoO$_3$ electrodes. k_{ET} for PTB7−Ag is low due to moderate values of J_{DA} combined with high values of ΔE, echoed in the high R_C of OFETs with the PTB7−Ag contact interface. In the case of PTB7−Th−Ag, a higher n is combined with a higher range of values of J_{DA}, which leads to higher values of k_{ET}. Contact resistance may vary according to applied voltage due to the effects of vertical charge transport induced by a lateral field. The gate voltage shifts energy levels at the interface, favoring charge injection to dope the channel, thereby reducing contact
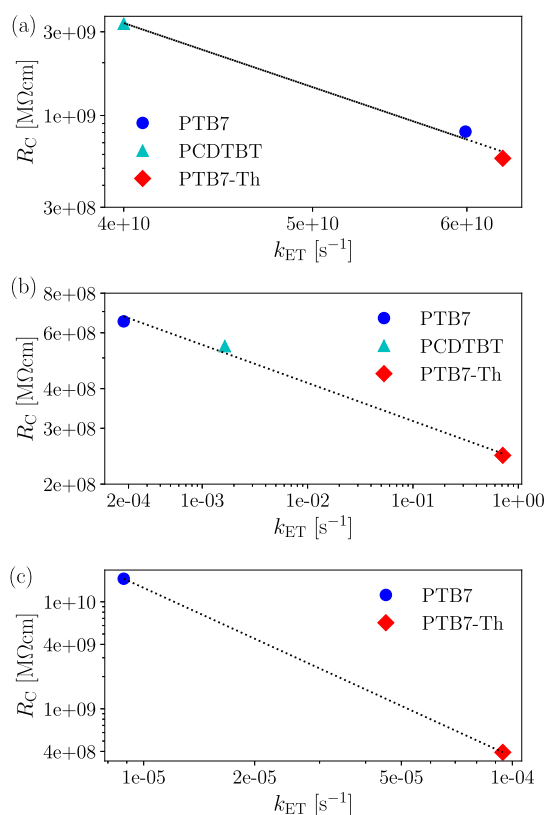
Figure 6. Correlation between electron transfer rate (k_{ET}) and the contact resistance (R_C) for OSC−electrode systems: (a) Au, (b) MoO$_3$, and (c) Ag electrodes, exhibiting the importance of energy levels and electronic coupling in governing device R_C.

interface with the monomer and electrode surface. Energy levels of the donor OSC and electrode were calculated, and the position of the vacant states on electrodes with respect to HOMO was compared for all systems. Further, the electronic coupling of vacant states of the electrode and HOMO of the OSC were calculated as it determines the feasibility of electron transfer. These values were used to calculate the electron transfer rate from the polymer to the electrode. The transfer rate was found to correlate strongly with the measured R_C, showing that a combination of energy levels of various states and electronic coupling between them determine the device R_C. Thus, by calculating k_{ET}, we understand the microscopic phenomenon at contact interfaces that govern device behavior and establish a method to evaluate contact interfaces for organic devices.

■ ASSOCIATED CONTENT

Ⓢ Supporting Information

The Supporting Information is available free of charge at https://pubs.acs.org/doi/10.1021/acsami.3c10260.

> Energy level diagram obtained by first-principles computations for contact interfaces with Au or Ag electrodes, mobility vs contact resistance plot, rate of electron transfer vs contact resistance diagram, and values of relevant computed and measured parameters for all OSC−electrode systems and respective OFETs (PDF)

■ AUTHOR INFORMATION

Corresponding Authors

Kalyani Patrikar − *Department of Chemistry, Indian Institute of Technology Gandhinagar, Gandhinagar, Gujarat 382355, India*; Email: kalyani.p@iitgn.ac.in

Anirban Mondal − *Department of Chemistry, Indian Institute of Technology Gandhinagar, Gandhinagar, Gujarat 382355, India*; ⓞ orcid.org/0000-0003-3029-8840; Email: amondal@iitgn.ac.in

Authors

V. Ramgopal Rao − *Birla Institute of Technology and Science, Pilani, Rajasthan 333031, India*

Dinesh Kabra − *Department of Physics, Indian Institute of Technology Bombay, Mumbai, Maharashtra 400076, India*; ⓞ orcid.org/0000-0001-5256-1465

Complete contact information is available at:
https://pubs.acs.org/10.1021/acsami.3c10260

Notes

The authors declare no competing financial interest.

■ ACKNOWLEDGMENTS

resistance. Here, we attempt to model the microscopic origin of contact resistance involving molecular interactions, and thus, the simulation parameters are voltage-independent. It is shown in Figure S3 that k predicts the trends in contact resistance for devices at $V_G = -10$ V for OFETs with Au electrodes as effects of gate voltage are uniform for all interfaces. Thus, Figure 6 demonstrates that k_{ET}, computed via the POD method for periodic systems, effectively measures R_C. k_{ET} evaluates the density of states available and their energy differences combined with the strength of electronic coupling of the states with donor HOMO. A combination of these factors determines the interface resistance. k_{ET} thus explains the microscopic phenomenon governing the interfacial electron transfer process and the effect of the microscopic physical processes on the device behavior.

4. CONCLUSIONS

Contact resistance measured for OFETs with different polymers exhibits similar trends regardless of electrodes, indicating that molecular properties play an essential role in determining the R_C of the device. Further, R_C values are different in the case of either electrode, suggesting that R_C depends on interfacial interactions between the polymer and electrodes. The microscopic phenomenon associated with the interface was studied by first-principles computations. It was observed that the orbital delocalization of HOMO of the OSC correlated strongly with trends in device R_C. The extent of delocalization was further explored by simulating aspects of the electron transfer process from HOMO of the monomer to vacant states of the electrode as occurs during charge injection in device operation. First-principles computations were carried out on a slice of contact

■ REFERENCES

(1) Tseng, C. W.; Huang, D. C.; Tao, Y. T. Organic Transistor Memory with a Charge Storage Molecular Double-floating-gate Monolayer. *ACS Appl. Mater. Interfaces* **2015**, 7, 9767−9775.

(2) Lee, J. I.; Kim, M.; Park, J. H.; Kang, B.; Lee, C. Y.; Park, Y. D. Metal−Organic Framework as a Functional Analyte Channel of Organic-Transistor-Based Air Pollution Sensors. *ACS Appl. Mater. Interfaces* **2021**, *13*, 24005−24012.

(3) Chauhan, A.; Jha, P.; Aswal, D.; Yakhmi, J. Organic Devices: Fabrication, Applications, and Challenges. *J. Electron. Mater.* **2022**, *51*, 447−485.

(4) Liu, C.; Xu, Y.; Noh, Y. Y. Contact Engineering in Organic Field-effect Transistors. *Mater. Today* **2015**, *18*, 79−96.

(5) Waldrip, M.; Jurchescu, O. D.; Gundlach, D. J.; Bittle, E. G. Contact Resistance in Organic Field-effect Transistors: Conquering the Barrier. *Adv. Funct. Mater.* **2020**, *30*, 1904576.

(6) Kim, C. H. Contact Resistance in Organic Transistors: Use it or Remove it. *Appl. Phys. Rev.* **2020**, *7*, 031306.

(7) Xu, Y.; Sun, H.; Noh, Y.-Y. Schottky Barrier in Organic Transistors. *IEEE Trans. Electron Devices* **2017**, *64*, 1932−1943.

(8) Natali, D.; Caironi, M. Charge Injection in Solution-Processed Organic Field-Effect Transistors: Physics, Models and Characterization Methods. *Adv. Mater.* **2012**, *24*, 1357−1387.

(9) Vázquez, H.; Gao, W.; Flores, F.; Kahn, A. Energy Level Alignment at Organic Heterojunctions: Role of the Charge Neutrality Level. *Phys. Rev. B: Condens. Matter Mater. Phys.* **2005**, *71*, 041306.

(10) Rockson, T. K.; Baek, S.; Jang, H.; Choi, G.; Oh, S.; Kim, J.; Cho, H.; Kim, S. H.; Lee, H. S. Engineering Asymmetric Charge Injection/extraction to Optimize Organic Transistor Performances. *ACS Appl. Mater. Interfaces* **2019**, *11*, 10108−10117.

(11) Wang, Z.; Waqas Alam, M.; Lou, Y.; Naka, S.; Okada, H. Enhanced Carrier Injection in Pentacene Thin-film Transistors by Inserting a MoO_3-doped Pentacene Layer. *Appl. Phys. Lett.* **2012**, *100*, 25.

(12) Patrikar, K.; Bothra, U.; Rao, V. R.; Kabra, D. Charge Carrier Doping as Mechanism of Self-assembled Monolayers Functionalized Electrodes in Organic Field Effect Transistors. *Adv. Mater. Interfaces* **2022**, *9*, 2101377.

(13) Zeng, J.; He, D.; Qiao, J.; Li, Y.; Sun, L.; Li, W.; Xie, J.; Gao, S.; Pan, L.; Wang, P.; et al. Ultralow Contact Resistance in Organic Transistors via Orbital Hybridization. *Nat. Commun.* **2023**, *14*, 324.

(14) Jung, S.; Jin, J. W.; Mosser, V.; Bonnassieux, Y.; Horowitz, G. A Compact Model and Parameter Extraction Method for a Staggered OFET with Power-law Contact Resistance and Mobility. *IEEE Trans. Electron Devices* **2019**, *66*, 4894−4900.

(15) Jung, S.; Lee, Y.; Plews, A.; Nejim, A.; Bonnassieux, Y.; Horowitz, G. Effect of Gaussian Disorder On Power-law Contact Resistance and Mobility in Organic Field-effect Transistors. *IEEE Trans. Electron Devices* **2021**, *68*, 307−310.

(16) Wang, Z.; Das, M.; Gutheil, C.; Osthues, H.; Strieth-Kalthoff, F.; Timmer, A.; Doltsinis, N. L.; Wang, W.; Chi, L.; Glorius, F. Surface Modification with a Fluorinated N-heterocyclic Carbene on Au: Effect on Contact Resistance in Organic Field-effect Transistors. *J. Mater. Chem. C* **2022**, *10*, 8589−8595.

(17) Stokbro, K.; Smidstrup, S. Electron Transport Across a Metal-organic Interface: Simulations using Nonequilibrium Green's Function and Density Functional Theory. *Phys. Rev. B: Condens. Matter Mater. Phys.* **2013**, *88*, 075317.

(18) Futera, Z.; Blumberger, J. Electronic Couplings for Charge Transfer Across Molecule/metal and Molecule/semiconductor Interfaces: Performance of the Projector Operator-based Diabatization Approach. *J. Phys. Chem. C* **2017**, *121*, 19677−19689.

(19) Marcus, R. A. On the Theory of Electron-transfer Reactions. VI. Unified Treatment for Homogeneous and Electrode Reactions. *J. Chem. Phys.* **1965**, *43*, 679−701.

(20) Kim, B.; Yeom, H. R.; Yun, M. H.; Kim, J. Y.; Yang, C. A. A Selenophene Analogue of PCDTBT: Selective Fine-Tuning of LUMO to Lower of the Bandgap for Efficient Polymer Solar Cells. *Macromolecules* **2012**, *45*, 8658−8664.

(21) Takagi, K.; Nagase, T.; Kobayashi, T.; Naito, H. Electrical Characterization of Thieno [3, 4-b] Thiophene and Benzodithiophene Copolymer Using Field-effect Transistor Configuration. *Jpn. J. Appl. Phys.* **2014**, *53*, 050305.

(22) Patrikar, K.; Jain, N.; Chakraborty, D.; Johari, P.; Rao, V. R.; Kabra, D. Influence of Pendant Group on Mobility of Organic Thin Film Transistor in Correlation with Reorganization Energy of Molecules. *Adv. Funct. Mater.* **2019**, *29*, 1805878.

(23) Nketia-Yawson, B.; Lee, J. H.; Jo, J. W. High-mobility Amorphous PTB7 Organic Transistors Enabled by High-capacitance Electrolyte Dielectric. *Appl. Phys. Lett.* **2021**, *119*, 042103.

(24) Beaupré, S.; Leclerc, M. PCDTBT: en Route for Low Cost Plastic Solar Cells. *J. Mater. Chem. A* **2013**, *1*, 11097−11105.

(25) Zheng, Y.; Wang, G.; Huang, D.; Kong, J.; Goh, T.; Huang, W.; Yu, J.; Taylor, A. D. Binary Solvent Additives Treatment Boosts the Efficiency of PTB7:PCBM Polymer Solar Cells to Over 9.5. *Sol. RRL* **2018**, *2*, 1700144.

(26) Wan, Q.; Guo, X.; Wang, Z.; Li, W.; Guo, B.; Ma, W.; Zhang, M.; Li, Y. 10.8% Efficiency Polymer Solar Cells Based on PTB7-Th and PC71BM via Binary Solvent Additives Treatment. *Adv. Funct. Mater.* **2016**, *26*, 6635−6640.

(27) Kim, C. H.; Hlaing, H.; Hong, J. A.; Kim, J. H.; Park, Y.; Payne, M. M.; Anthony, J. E.; Bonnassieux, Y.; Horowitz, G.; Kymissis, I. Decoupling the Effects of Self-assembled Monolayers on Gold, Silver, and Copper Organic Transistor Contacts. *Adv. Mater. Interfaces* **2015**, *2*, 1400384.

(28) Kumaki, D.; Umeda, T.; Tokito, S. Reducing the Contact Resistance of Bottom-contact Pentacene Thin-film Transistors by Employing a MoO_x Carrier Injection Layer. *Appl. Phys. Lett.* **2008**, *92*, 1.

(29) Kondov, I.; Čížek, M.; Benesch, C.; Wang, H.; Thoss, M. Quantum Dynamics of Photoinduced Electron-Transfer Reactions in Dye-Semiconductor Systems: First-Principles Description and Application to Coumarin 343-TiO_2. *J. Phys. Chem. C* **2007**, *111*, 11970−11981.

(30) Hush, N. S. Adiabatic Rate Processes at Electrodes. I. Energy-charge Relationships. *J. Chem. Phys.* **1958**, *28*, 962−972.

(31) Ablat, A.; Kyndiah, A.; Houin, G.; Alic, T. Y.; Hirsch, L.; Abbas, M. Role of Oxide/metal Bilayer Electrodes In Solution Processed Organic Field Effect Transistors. *Sci. Rep.* **2019**, *9*, 6685.

(32) Hohenberg, P.; Kohn, W. Inhomogeneous Electron Gas. *Phys. Rev.* **1964**, *136*, B864−B871.

(33) Kohn, W.; Sham, L. J. Self-consistent Equations Including Exchange and Correlation Effects. *Phys. Rev.* **1965**, *140*, A1133−A1138.

(34) Hutter, J.; Iannuzzi, M.; Schiffmann, F.; VandeVondele, J. CP2K: Atomistic Simulations of Condensed Matter Systems. *Wiley Interdiscip. Rev. Comput. Mol. Sci.* **2014**, *4*, 15−25.

(35) VandeVondele, J.; Krack, M.; Mohamed, F.; Parrinello, M.; Chassaing, T.; Hutter, J. Quickstep: Fast and Accurate Density Functional Calculations using a Mixed Gaussian and Plane Waves Approach. *Comput. Phys. Commun.* **2005**, *167*, 103−128.

(36) Perdew, J. P.; Burke, K.; Ernzerhof, M. Generalized Gradient Approximation Made Simple. *Phys. Rev. Lett.* **1996**, *77*, 3865−3868.

(37) Hartwigsen, C.; Goedecker, S.; Hutter, J. Relativistic Separable Dual-space Gaussian Pseudopotentials from H to Rn. *Phys. Rev. B: Condens. Matter Mater. Phys.* **1998**, *58*, 3641−3662.

(38) Goedecker, S.; Teter, M.; Hutter, J. Separable Dual-space Gaussian Pseudopotentials. *Phys. Rev. B: Condens. Matter Mater. Phys.* **1996**, *54*, 1703−1710.

(39) Li, W.-L.; Chen, K.; Rossomme, E.; Head-Gordon, M.; Head-Gordon, T. Optimized Pseudopotentials and Basis Sets for Semiempirical Density Functional Theory for Electrocatalysis Applications. *J. Phys. Chem. Lett.* **2021**, *12*, 10304−10309.

(40) Köhler, A.; Bässler, H. *Electronic Processes in Organic Semiconductors: An Introduction*; John Wiley & Sons, 2015, p 156.

(41) Frisch, M. J.; et al. *Gaussian 03*; Gaussian, Inc.: Wallingford, CT, 2004.

(42) Becke, A. D. A. A new inhomogeneity parameter in density-functional theory. *J. Chem. Phys.* **1998**, *109*, 2092−2098.

(43) Lee, C.; Yang, W.; Parr, R. G. Development of the Colle-Salvetti correlation-energy formula into a functional of the electron density. *Phys. Rev. B: Condens. Matter Mater. Phys.* **1988**, *37*, 785−789.

(44) Perdew, J. P. Density-functional Approximation for the Correlation Energy of the Inhomogeneous Electron Gas. *Phys. Rev. B: Condens. Matter Mater. Phys.* **1986**, *33*, 8822−8824.

(45) Ditchfield, R.; Hehre, W. J.; Pople, J. A. Self-consistent Molecular-orbital Methods. IX. An Extended Gaussian-type Basis for Molecular-orbital Studies of Organic Molecules. *J. Chem. Phys.* **1971**, *54*, 724−728.

(46) Petersson, a.; Bennett, A.; Tensfeldt, T. G.; AlLaham, M. A.; Shirley, W. A.; Mantzaris, J. A complete Basis Set Model Chemistry. I. The Total Energies of Closed-shell Atoms and Hydrides of the First-row Elements. *J. Chem. Phys.* **1988**, *89*, 2193−2218.

(47) Klauk, H.; Zschieschang, U.; Pflaum, J.; Halik, M. Ultralow-power Organic Complementary Circuits. *Nature* **2007**, *445*, 745−748.

(48) Zhao, D.; Cui, Q.; Zhang, X.; Ji, H.; Liu, X.; Qin, L.; Hu, Y.; Hou, Y.; Hu, Y.; Lou, Z.; et al. Improving the Mobility of DA Polymer PTB7-Th Thin Film Field-effect Transistors Through Organic Salt Doping. *Org. Electron.* **2023**, *120*, 106863.

(49) Choudhury, A.; Gupta, R. K.; Garai, R.; Iyer, P. K. Tuning Polymer Semiconductor Morphology through Additive Engineering for a Stable Phototransistor. *ACS Appl. Electron. Mater.* **2021**, *3*, 5393−5401.

(50) Hu, Y.; Li, G.; Chen, Z. The Importance of Contact Resistance in High-Mobility Organic Field-effect Transistors Studied by Scanning Kelvin Probe Microscopy. *IEEE Electron Device Lett.* **2018**, *39*, 276−279.